# Sensor placement in nuclear reactors based on the generalized empirical interpolation method

J.-P. Argaud, B. P Bouriquet, F. de Caso, Helin Gong, Yvon Maday, Olga Mula

# Sensor placement in nuclear reactors based on the Generalized Empirical Interpolation Method

J.-P. Argaud[a], B. Bouriquet[a], F. de Caso[a], H. Gong[a,b], Y. Maday[b,c,d], O. Mula[e]

[a] *Électricité de France, R&D, 7 boulevard Gaspard Monge, 91120 Palaiseau, France.*
[b] *Sorbonne Universités, UPMC Univ Paris 06 and CNRS UMR 7598, Laboratoire Jacques-Louis Lions, F-75005, Paris, France.*
[c] *Institut Universitaire de France.*
[d] *Division of Applied Mathematics, Brown University, Providence RI, USA.*
[e] *Université Paris-Dauphine, PSL Research University, CNRS, UMR 7534, CEREMADE, 75016 Paris, France.*

**Abstract**

In this paper, we apply the so-called generalized empirical interpolation method (GEIM) to address the problem of sensor placement in nuclear reactors. This task is challenging due to the accumulation of a number of difficulties like the complexity of the underlying physics and the constraints in the admissible sensor locations and their number. As a result, the placement, still today, strongly relies on the know-how and experience of engineers from different areas of expertise. The present methodology contributes to making this process become more *systematic* and, in turn, simplify and accelerate the procedure.

*Keywords:* generalized empirical interpolation method, sensor placement, data assimilation, nuclear safety, greedy algorithm
*PACS:* 02.30.Jr, 02.30.Mv, 02.60.Cb, 02.60.Ed, 02.60.Gf
*2010 MSC:* 65D05, 41A29, 65Z05, 65N99, 93B15

## 1. Introduction

Nowadays, the production of nuclear energy is done under very high safety standards where tight criteria must be satisfied both at design and operation levels. What is essentially required is the accurate knowledge of significant quantities like temperature, neutron flux, power, irradiation or fluence. The quantities can be global outputs like the maximum or average temperature or the total generated power but the knowledge of more detailed information like temperature, flux and/or power maps in the whole reactor may also be required. The knowledge of any of these quantities is accessed either through the study of parametrized models and/or through measurement data collected from the reactor itself. In very general lines, the usual way to work with models and data at design and operation levels is the following:

- At design stages, the goal is essentially to first find the most realistic model for the physics' core and then optimize the parameters of the model to find the safest core

configurations. At this stage, if measured data from previous experiments are at reach, they are only used to find the model.

- At the operation level, the information is primarily obtained via sensor measurements. Their placement has to be carefully optimized in order to retrieve as much information as possible while the reactor is running.

In all these modelling and optimization steps, the experience of engineers plays a crucial role in order to find acceptable configurations. Even more, due to the complexity of the physics, it is sometimes necessary to combine the expertise of engineers from different fields and the modelling/optimization process might require several iterations between experts before satisfying all the desired criteria. In this context, this paper is a contribution to making these tasks become more *systematic*. For this, we apply a novel methodology from the fields of data assimilation and model order reduction to the field of reactor simulations. For a given quantity of interest, the method provides a quick approximation of it by combining the measurement data and the knowledge of a parametrized model. The key idea is to do the reconstruction on a well chosen finite dimensional space of *reduced* dimension. The basis functions of this space are solutions to the model problem for appropriately chosen parameter values. This idea, which is the root of reduced order modeling techniques such as reduced basis, constitutes the reduced modelling part of our approach. An overview of reduced bases can be found in the reference books [1, 2] and a summary on some relevant applications to nuclear engineering is given later on in the paper. With respect to these works, the new main ingredient that we bring is the combination of this idea with data assimilation. This is done via the Empirical Interpolation Method (EIM, [3]) which we will use in its generalized version (GEIM, see [4, 5]). In this approach, the approximation in the space of reduced dimension is defined in such a way that the measures on the approximant coincide with the measured data. Two features of this methodology which might be of interest to the community of nuclear engineering are the following:

- The information from the model and the measurements is incorporated *simultaneously* and not in a sequential manner like in the classical procedures in nuclear engineering.

- Since the approximation is done on a space of small dimension (dimension 20 or 30 is usually enough in many cases), its computation is very quick. This could be helpful to accelerate some steps at design and operation stages.

We would like to emphasize that GEIM belongs to a broader class of recovery methods which gathers other approaches like the PBDW methodology of [6] where the use of data allows not only to reconstruct the quantities of interest, but also to correct the possible bias in the mathematical model. Here we shall not use this feature and assume that the mathematical model is perfect, that is, there exists an (unknown) value of the parameter such that the model represents very accurately the true running situation. The whole class is subject of current active research in the community of applied mathematics (see, e.g., [7, 8, 9, 10]) since it carries potential to address in a unified methodology different types of

inverse or uncertainty quantification problems arising in a large variety of physical systems. Among the possible applications of the method to the field of reactor physics stand

(i) the search for optimal sensor locations to measure certain quantities of interest during the operation of the core,

(ii) the acceleration in the search for optimally safe and/or efficient core configurations since GEIM gives a quick reconstruction of the quantities of interest.

Much more ambitious is the possibility to take into account the accuracy of the sensors in the placement selection. Indeed one could be interested in using few, very accurate, sensors and more, less accurate ones. The natural questions are then to place them in an optimal way. Another related question is: given a certain budget, what is the best location/quality/number of sensors to recover the best approximation. This question is difficult to answer in general but a recent investigation on this topic can be found in [11]. At any rate, we emphasize that the method cannot completely replace the experience of experts of the field. It should be seen as a tool to assist them in doing these tasks more efficiently and especially in a more *systematic* way.

Since the number of potential applications is relatively broad, in this paper we restrict ourselves to idea (i). Our main contribution is to give numerical evidence that GEIM can help to place sensors in order to best reconstruct physical quantities such as the neutronic flux or the power in the whole core. We present results on three different examples of nuclear cores which are relevant in the field of neutronics. One of them involves the real geometry of a Pressurized Water Reactor operated by the French electricity company Électricité de France (EDF). To explain our computations, we start by presenting in section 2 the methodology and greedy algorithm of GEIM in general terms. We next explain in section 3 how we have applied the method to our case of interest where we work with a parametric diffusion equation as a model for the neutronics in a nuclear reactor. The presentation of GEIM in these two sections is deliberately oriented towards physicists and engineers which are not necessarily experts in the field of model order reduction. The neutron flux and the power have been taken as examples of quantities of interest but we hope that readers from other fields will be able to extrapolate the idea to their own problems. A more mathematical presentation of the algorithm can be found in [5, 10] and the reader familiar with the methodology can skip section 2. We differ the presentation of the state of the art on model order reduction techniques applied to nuclear reactor simulations until the end of section 3 to let the unfamiliar reader learn the main ideas of GEIM and model order reduction first. Section 4 gives our numerical results on three different examples of increasing difficulty and degree of reality. They are respectively in 1, 2 and 3 spatial dimensions. The results for the examples in 1 and 2 dimensions are an extension of the numerical results announced in [12] and we put here special emphasis on the sensor placement rather than on stability considerations. We finish the article by briefly explaining generalizations of GEIM, current theoretical challenges and new perspectives regarding nuclear physics applications (see Section 5).

## 2. The Generalized Empirical Interpolation Method

### *2.1. Preliminaries*

By way of preliminaries, we introduce the mathematical notations used throughout this paper. Let $\mathcal{X}$ be a Banach space defined over a physical domain $\mathcal{R} \subset \mathbb{R}^d$ $(d \geq 1)$ and let $\|\cdot\|$ be the associated norm. In our case $\mathcal{R}$ will be the reactor domain and $\mathcal{X}$ will be either $L^2(\mathcal{R})$, $L^\infty(\mathcal{R})$ or a product of these spaces.

### *2.2. Rationale of the Generalized Empirical Interpolation Method*

In order to reconstruct the state $f \in \mathcal{X}$ of a physical quantity, we assume that we have access to two types of information:

i) Information coming from measurements collected directly from the physical system. In the following, we model sensors with linear functionals $\sigma \in \mathcal{X}'$ parametrized by the position $x \in \mathcal{X}$ and the quantity $\sigma(f, x)$ denotes the measurement value given from a sensor located in $x \in \mathcal{R}$. The linear functionals can be chosen as Dirac masses, in which case the measurements are pointwise evaluations of $f$ at some points $x \in \mathcal{R}$,

$$\sigma(f, x) = \delta_x(f) = f(x).$$

A perhaps more realistic option is to work with local averages centered around some point $x$. If $D(x)$ is a neighborhood of $x$ and $g$ is a radial function, one can work with

$$\sigma(f, x) = \int_{D(x)} f(t)g(x - t)\ \mathrm{d}t.$$

In our numerical experiments, we work either with Dirac masses or local averages depending on the test case.

ii) An information coming from a physical model, which generally comes in the form of a parametric partial differential equation (PDE). We assume that $f$ is the solution to

$$\mathcal{A}(f, \mu) = 0, \tag{2.1}$$

where $\mathcal{A}$ is a differential operator defined in $\mathcal{X}$ and $\mu \in \mathbb{R}^p$ is a vector of $p \geq 1$ parameters. In our case, we assume that for any $\mu$, there exists a unique solution $f(\cdot, \mu) \in \mathcal{X}$ to problem (2.1). However, the particular parameter $\mu$ that best describes the system under consideration is in general not well known. Instead, one usually knows that the parameters may lie in some range $\mathcal{D} \subset \mathbb{R}^p$ so that the information from the parametrized model is that our function $f$ of interest belongs to the set

$$\mathcal{M}_f \coloneqq \{f(\cdot, \mu)\ : \mu \in \mathcal{D}\}, \tag{2.2}$$

which is called the manifold of states. For certain classes of PDEs and for a given target accuracy $\varepsilon > 0$, it is possible to approximate the elements of $\mathcal{M}_f$ with $n$-dimensional linear spaces $X_n$ such that

$$\mathrm{dist}(\mathcal{M}_f, V_n) \coloneqq \max_{u \in \mathcal{M}_f} \min_{v \in V_n} \|u - v\| \leq \varepsilon,$$

and where the dimension $n = n(\varepsilon)$ increases moderately with the accuracy $\varepsilon$ (see [13]). In other words, one can find spaces $X_n$ of reduced dimension which approximate $\mathcal{M}_f$ at high accuracy. The underlying reason for having this property is that the Kolmogorov $n$-width of the manifold

$$d_n(\mathcal{M}, \mathcal{X}) \coloneqq \inf_{\substack{X_n \subset \mathcal{X} \\ \dim X_n \leq n}} \operatorname{dist}(\mathcal{M}_f, V_n)$$

has a fast decay in $n$. This quantity measures the minimal approximation error of $\mathcal{M}$ with linear subspaces of dimension less than or equal to $n$. Therefore, if it decays quickly in $n$, there is room to find spaces of reduced dimension with good approximation properties. This desirable behavior of $(d_n(\mathcal{M}, \mathcal{X}))_{n \geq 1}$ is satisfied for certain PDEs like elliptic ones thanks to the regularity of $f(\cdot, \mu)$ in $\mu$ (see [14, 15, 16]). One technique to build these spaces are reduced basis methods, which use a greedy algorithm to select functions $f(\cdot, \mu_i)$ for appropriately chosen parameters $\mu_i$ and then define $X_n \coloneqq \operatorname{span}\{f(\cdot, \mu_i) \, : \, i = 1, \dots, n\}$.

GEIM combines measured data and a reduced space as follows. We first run a greedy algorithm which selects

- a set of functions $\{f(\cdot, \mu_1), \cdots, f(\cdot, \mu_n)\}$ from the manifold $\mathcal{M}_f$. These functions will span our reduced basis $X_n \coloneqq \operatorname{span}\{f(\cdot, \mu_i) \, : \, i = 1, \dots, n\}$. For convenience, we will sometimes work with another basis of $X_n$ spanned by functions $q_i \in X_n$ which are built from linear combinations of the $f(\cdot, \mu_i)$. Their exact form is given in section 2.3.

- a set of locations $x_1, \dots, x_n \in \mathcal{R}$ for the sensors. The locations are searched among all admissible positions $x \in \mathcal{R}_{\text{admissible}}$. Mathematically, this is expressed by saying that we search for sensors $\sigma(\cdot, x)$ among a dictionary $\Sigma \coloneqq \{\sigma(\cdot, x) \; x \in \mathcal{R}_{\text{admissible}}\}$ of potential candidates. One technical condition which is required is the following *unisolvence property*: if $f \in \mathcal{X}$ is such that $\sigma(f) = 0, \forall \sigma \in \Sigma$, then $f = 0$.

Once $X_n$ and the sensor locations are selected, we approximate any function $f(\cdot, \mu) \in \mathcal{M}_f$ with

$$\mathcal{J}_n[f](\mu) \coloneqq \sum_{j=1}^{n} c_j(\mu) q_j \in X_n \tag{2.3}$$

The $c_j(\mu)$ are coefficients which depend on the parameters $\mu$. They are computed using measurement information by imposing the interpolating conditions

$$\sigma\left(f(\cdot, \mu), x_k\right) = \sigma\left(\mathcal{J}_n[f](\mu), x_k\right), \; k \in \{1, \dots, n\}, \tag{2.4}$$

where we see that the coefficients $(c_1, \dots, c_n)$ are the solution of a $n \times n$ linear system of equations. The reconstruction gives enough accuracy for a small dimension $n$ of $X_n$. We refer to [5, 10] for the mathematical analysis of the approach.

The next section explains how the greedy algorithm is exactly defined. Before moving to it, we would like to emphasize that, in this approach, the mathematical model is assumed to be perfect in the sense indicated above. Other approaches like the PBDW methodology of [6] allow to correct the possible model bias.

*2.3. GEIM greedy algorithm*

We start by finding a parameter $\mu_1$ in $\mathcal{D}$ such that

$$\|f(\cdot,\mu_1)\| = \max_{\mu\in\mathcal{D}} \|f(\cdot,\mu)\|. \tag{2.5}$$

Note that several parameters $\mu$ might maximize the function $\mu \to \|f(\cdot,\mu)\|$. In this case, $\mu_1$ is picked among the set of maximizers. The state $f(\cdot,\mu_1)$ defines $X_1 = \text{span}\{f(\cdot,\mu_1)\}$. The first sensor location $x_1$ is one of possibly multiple maximizers such that

$$|\sigma\left(f(\cdot,\mu_1),x_1\right)| = \max_{x\in\mathcal{R}} |\sigma\left(f(\cdot,\mu_1),x\right)|. \tag{2.6}$$

To facilitate the practical computation of the generalized interpolant, we do a change of basis in $X_1$. Instead of working with $f(\cdot,\mu_1)$ as basis function, we use

$$q_1 = \frac{f(\cdot,\mu_1)}{\sigma(f(\cdot,\mu_1),x_1)}.$$

For any $\mu \in \mathcal{D}$, the generalized interpolant of $f(\cdot,\mu)$ is

$$\mathcal{J}_1[f](\mu) = c_1(\mu)q_1 \tag{2.7}$$

and $c_1(\mu)$ is found with the interpolating conditions (2.4) for $n = 1$. We then proceed by induction. Assume that, for a given $M \geq 1$, we have selected a set of states $\{f(\cdot,\mu_j)\}_{j=1}^M$ and the associated basis functions $\{q_1, q_2, \ldots, q_M\}$ that span $X_M$. Assume also that we have chosen positions $x_1, \ldots, x_M$ to locate the first $M$ sensors. The generalized interpolant is assumed to be well defined by (2.3) for $n = M$, i.e.,

$$\mathcal{J}_M[f](\mu) \coloneqq \sum_{j=1}^{M} c_j(\mu)q_j.$$

The coefficients $c_j(\mu)$, $j \in \{1,\ldots,M\}$, are given by the interpolation problem (2.4) for $n = M$, i.e.,

$$\begin{cases} \text{Find } \{c_j(\mu)\}_{j=1}^M \text{ such that:} \\ \sum_{j=1}^{M} c_j(\mu)B_{k,j} = \sigma\left(f(\cdot,\mu),x_k\right), \ \forall k \in \{1,\ldots,M\}. \end{cases}$$

where $B_{k,j}$ are the coefficients of the $M \times M$ matrix $B := \left(\sigma(q_j,x_k)\right)_{1\leq k,j\leq M}$. We now define $f(\cdot,\mu_{M+1})$ such that

$$\|(f - \mathcal{J}_M[f])(\mu_{M+1})\| = \max_{\mu\in\mathcal{D}} \|(f - \mathcal{J}_M[f])(\mu)\|, \tag{2.8}$$

and $x_{M+1}$ such that

$$|\sigma\left(\left(f - \mathcal{J}_M[f]\right)(\mu_{M+1}),x_{M+1}\right)| = \max_{x\in\mathcal{R}} |\sigma\left(\left(f - \mathcal{J}_M[f]\right)(\mu_{M+1}),x\right)|. \tag{2.9}$$

Like in the case $M = 1$, we might have several maximizers and, in this case, we just pick $\mu_{M+1}$ and $x_{M+1}$ as one of them. The next basis function is then

$$q_{M+1} = \frac{(f - \mathcal{J}_M[f])(\mu_{M+1})}{\sigma\left((f - \mathcal{J}_M[f])(\mu_{M+1}), x_{M+1}\right)}$$

We finally set $X_{M+1} = \text{span}\{f(\cdot, \mu_j)\}_{j=1}^{M+1} = \text{span}\{q_j\}_{j=1}^{M+1}$ and the generalized interpolant of $f(\cdot, \mu)$ at dimension $M + 1$ is defined by formula (2.3) with $n = M + 1$. It satisfies the interpolating conditions (2.4) for the sensors located at the $M + 1$ positions given by the algorithm.

It has been proven in [10] that for any $n \geq 1$, the set $\{q_1, \ldots, q_n\}$ is linearly independent and that this interpolation procedure is well-posed in $\mathcal{X}$. This follows from the fact that the matrix $B$ is lower triangular with diagonal entries equal to 1.

Let us now make several remarks.

i) The particular case where $\mathcal{X} = L^\infty(\mathcal{R})$ and the dictionary $\Sigma$ is composed of Dirac masses is called EIM (and not Generalized EIM). This variant is the first one presented in the literature (see [3]).

ii) $\mathcal{D}$ is a set containing parameters in a continuous range so, in practice, it is not possible to compute maximum values over $\mathcal{D}$ as required in formulas (2.5) and (2.8). The same applies for the computation of the maximum over $x \in \mathcal{R}$ in (2.6) and (2.9). This is the reason why it is necessary to work with discrete subsets $\mathcal{D}^{(\text{training})}$, $\mathcal{R}^{(\text{training})}$ of $\mathcal{D}$ and $\mathcal{R}$. They have to be fine enough so that the maximum over $\mathcal{D}^{(\text{training})}$ (resp. $\mathcal{R}^{(\text{training})}$) is representative of the maximum over $\mathcal{D}$ (resp. $\mathcal{R}$).

iii) In practice, problem (2.1) is solved with a numerical scheme that we denote by SOLVE and which yields an approximation $\bar{f}(\cdot, \mu)$ of $f(\cdot, \mu)$,

$$\bar{f}(\cdot, \mu) = \text{SOLVE}\left(\mathcal{F}\left(f, \mu\right) = 0\right).$$

For a given $\mu \in \mathcal{D}^{(\text{training})}$, note that $f(\cdot, \mu)$ is the *exact* solution to the PDE (2.1). So $f(\cdot, \mu)$ is not known exactly but only via an approximation $\bar{f}(\cdot, \mu)$ coming from $\text{SOLVE}\left(\mathcal{F}\left(f, \mu\right) = 0\right)$. $\bar{f}(\cdot, \mu)$ is the quantity that is considered in the practical implementation of the algorithm. For any $\bar{\mu} \in \mathcal{D}^{(\text{training})}$, $\bar{f}(\cdot, \mu)$ is called a snapshot and

$$\mathcal{M}_{\mathcal{D}^{(\text{training})}} \coloneqq \{\bar{f}(\cdot, \mu) \ : \ \mu \in \mathcal{D}^{(\text{training})}\}$$

is called the set of snapshots. It is intended to be representative enough of the set $\mathcal{M}_f$ defined in (2.2).

The discretizations ($\mathcal{D}^{(\text{training})}$, $\mathcal{R}^{(\text{training})}$, $\bar{f}$) yield an implementable version of the greedy algorithm. If they are fine enough, the algorithm provides, up to a factor, a convergence rate which is the same as the greedy algorithm with ($\mathcal{D}$, $\mathcal{R}$, $f$), see [10]. However, quantifying how fine these discretizations should be is a difficult task. Even more difficult is finding a

systematic way of building the discretizations. One result in this direction is lemma 1 of [10], which quantifies how much one needs to refine $\mathcal{D}^{(\text{training})}$ and $\mathcal{R}^{(\text{training})}$ at each step $M$ of the algorithm. However, the result is difficult to use for practical purposes. Another relevant reference is [17] where the authors propose an approach to refine $\mathcal{D}^{(\text{training})}$ by adapting the local approximation spaces to the local anisotropic behavior in the parameter space, thus expected to be representative enough of the set $\mathcal{M}_f$.

## 3. Application of GEIM to reconstruct the flux and power of a nuclear reactor core

### *3.1. Physical model and remarks on how to apply GEIM*

In this work, the neutron flux $\phi$ is modeled with the two-group neutron diffusion equation with null flux boundary conditions. So $\phi$ has two energy groups $\phi = (\phi_1, \phi_2)$. Index 1 denotes the high energy group and 2 the thermal energy one. The flux is the solution to the following eigenvalue problem (see [18])

$$\text{Find } (\lambda, \phi) \in \mathbb{C} \times (L^\infty(\mathcal{R}) \times L^\infty(\mathcal{R})) \text{ such that for all } x \in \mathcal{R},$$

$$\begin{cases} -\nabla\left(D_1 \nabla \phi_1\right) + (\Sigma_{a,1} + \Sigma_{s,1\to 2})\phi_1 = \lambda\left(\chi_1 \nu \Sigma_{f,1}\phi_1 + \chi_1 \nu \Sigma_{f,2}\phi_2\right) \\ -\nabla\left(D_2 \nabla \phi_2\right) + D_1\phi_2 - \Sigma_{s,1\to 2}\phi_1 = \lambda\left(\chi_2 \nu \Sigma_{f,1}\phi_1 + \chi_2 \nu \Sigma_{f,2}\phi_2\right), \end{cases} \tag{3.1}$$

with

$$\phi_i|_{\partial\mathcal{R}} = 0 \quad \text{for } i = 1,\, 2.$$

The coefficients involved are the following:

- $D_i$ is the diffusion coefficient of group $i$ with $i \in \{1, 2\}$.
- $\Sigma_{a,i}$ is the macroscopic absorption cross section of group $i$.
- $\Sigma_{s,1\to 2}$ is the macroscopic scattering cross section from group 1 to 2.
- $\Sigma_{f,i}$ is the macroscopic fission cross section of group $i$.
- $\nu$ is the average number of neutrons emitted per fission.
- $\chi_i$ is the fission spectrum of group $i$.

The generated power is

$$P \coloneqq \nu\Sigma_{f,1}\phi_1 + \nu\Sigma_{f,2}\phi_2. \tag{3.2}$$

We next make some comments on the coefficients and recall well-posedness results of the eigenvalue problem (3.1). First of all, the first four coefficients ($D_i$, $\Sigma_{a,i}$, $\Sigma_{s,1\to 2}$ and $\Sigma_{f,i}$) might depend on the spatial variable. In the following, we assume that they are either constant or piecewise constant so that our set of parameters is

$$\mu = \{D_1, D_2, \Sigma_{a,1}, \Sigma_{a,2}, \Sigma_{s,1\to 2}, \nu, \Sigma_{f,1}, \Sigma_{f,2}, \chi_1, \chi_2\}. \tag{3.3}$$

By abuse of notation, in (3.3) we have written $D_i$ to denote the set of values that this coefficient might take in space and similarly for the other parameters.

Under some mild conditions on the parameters $\mu$, the eigenvalue $\lambda_{\max}$ with the largest module is simple, real and strictly positive (see [19, Chapter XXI]). The associated eigenfunction $\phi$ is also real and positive at every point $x \in \mathcal{R}$ and it is what is classically called the flux. In neutronics, it is customary to work with the inverse of $\lambda_{\max}$, which is called the multiplication factor

$$k_{\text{eff}} \coloneqq 1/\lambda_{\max}. \tag{3.4}$$

Therefore $k_{\text{eff}}$ is not a parameter in our setting because, for each value of the parameters $\mu$, $k_{\text{eff}}$ is determined by the solution to the eigenvalue problem. In the computations of Section 4, the numerical scheme SOLVE to compute the eigenvalue $1/k_{\text{eff}}$ is based on the well-known power method (see, e.g., [18]). The spatial approximation uses $\mathbb{P}_1$ finite elements of a grid of size $h$ (this value will be specified later in Section 4).

If the parameters of our diffusion model range in, say,

$$D_1 \in [D_{1,\min}, D_{1,\max}],\ D_2 \in [D_{2,\min}, D_{2,\max}], \dots, \chi_2 \in [\chi_{2,\min}, \chi_{2,\max}],$$

then

$$\mathcal{D} \coloneqq [D_{1,\min}, D_{1,\max}] \times \cdots \times [\chi_{2,\min}, \chi_{2,\max}] \tag{3.5}$$

and the set of all possible states of the flux and power is given by

$$\mathcal{M}_{\phi_1,\phi_2,P} \coloneqq \{(\phi_1, \phi_2, P)(\mu)\ :\ \mu \in \mathcal{D}\}, \tag{3.6}$$

which is the manifold of solutions of our problem. It is composed of vectorial quantities $(\phi_1, \phi_2, P)(\mu)$. Running GEIM in this case leads to various possibilities. First we could work on a tensor product space $\mathcal{X}^3$, with measurements on the triplet $(\phi_1, \phi_2, P)$, or on $\phi_1$, $\phi_2$, $P$ separately, letting the algorithm select which quantity is best to include at each step $n$ of the greedy algorithm. One could also view the problem differently and define three independent manifolds

$$\begin{cases} \mathcal{M}_{\phi_1} \coloneqq \{\phi_1(\mu)\ :\ \mu \in \mathcal{D}\} \\ \mathcal{M}_{\phi_2} \coloneqq \{\phi_2(\mu)\ :\ \mu \in \mathcal{D}\} \\ \mathcal{M}_{P} \coloneqq \{P(\mu)\ :\ \mu \in \mathcal{D}\} \end{cases} \tag{3.7}$$

for which we run three separate GEIM algorithms. To go either one of these two above ways we need to have access to sensor measurements. For this reason, it is preferable to consider the manifold (3.6) and devise a reconstruction strategy where only thermal flux measurements are taken. We will follow the approach of [5] where the authors reconstruct the velocity and pressure of a fluid by using pressure measurements only. We describe how to adapt the strategy to the current neutronics problem in the next section. We also take into account that there are usually restrictions on the locations to place the sensors in the reactor $\mathcal{R}$. A typical situation is that they can only be placed in the subdomain of $\mathcal{R}$ corresponding to the core $\mathcal{R}_{\text{core}}$ but there are no sensors in the reflector $\mathcal{R}_{\text{refl}}$.

*3.2. A GEIM algorithm for the neutronics problem*

In the following $\mathcal{C}$ denotes a subdomain of the reactor $\mathcal{R}$ and we assume that $\overline{\mathcal{R}} = \overline{\mathcal{R}}_{\text{core}} \cup \overline{\mathcal{R}}_{\text{refl}}$ and $\mathcal{R}_{\text{core}} \cap \mathcal{R}_{\text{refl}} = \emptyset$. To work with the manifold (3.6), we modify the greedy algorithm of section 2.3 to approximate the flux and power of $\mathcal{M}_{\phi_1,\phi_2,P}$ when:

- we only use thermal flux measurements (related to $\phi_2$),
- the sensors can only be placed in a partial region $\mathcal{C}$ of the reactor, e.g., $\mathcal{C} = \mathcal{R}_{\text{core}}$ or $\mathcal{C} = \mathcal{R}$.

The approach requires to assume that:

- the Kolmogorov $n$-width of $\mathcal{M}_{\phi_1,\phi_2,P}$ decays fast,
- the thermal flux sensors satisfy the *unisolvence property*,
- for any given $\mu \in \mathcal{D}$, the knowledge of $\phi_2(\mu)$ allows to uniquely reconstruct $\phi_1(\mu)$ such that $\phi = (\phi_1,\, \phi_2)(\mu)$ is the unique positive eigenfunction of the eigenvalue problem (3.2) for the given parameter $\mu$. This property is satisfied if we assume that the mapping $\mu \mapsto \phi_2(\mu)$ is one to one. This is a strong hypothesis and, in the following, we assume that we are in a regime $\mathcal{D}$ of parameters where this is true (we will be able to confirm this in our numerical examples). We explain why this assumption is necessary at the end of the section.

We start by defining $\mu_1$ as the quantity maximizing

$$\max\left(\max_{\mu\in\mathcal{D}} \|\phi_1(\mu)\|,\ \max_{\mu\in\mathcal{D}} \|\phi_2(\mu)\|,\ \max_{\mu\in\mathcal{D}} \|P(\mu)\|\right). \tag{3.8}$$

This yields $X_1^1 = \text{span}\{\phi_1(\mu_1)\}$, $X_1^2 = \text{span}\{\phi_2(\mu_1)\}$ and $X_1^P = \text{span}\{P(\mu_1)\}$. The first sensor location $x_1$ is now the one such that

$$|\sigma(\phi_2, x_1)| = \max_{x\in\mathcal{C}} |\sigma(\phi_2, x)|. \tag{3.9}$$

For any $\mu \in \mathcal{D}$, we can then define $\mathcal{J}_1[\phi_2](\mu)$ as in the previous algorithm, i.e.

$$\mathcal{J}_1[\phi_2](\mu) \coloneqq c_1^{(2)}(\mu) q_1^{(2)}. \tag{3.10}$$

Expressing $\mathcal{J}_1[\phi_2](\mu)$ with the snapshot $\phi_2(\mu_1)$, we equivalently have

$$\mathcal{J}_1[\phi_2](\mu) \coloneqq d_1(\mu)\phi_2(\mu_1). \tag{3.11}$$

Since we no longer have at hand either $\sigma(\phi_1, x_1)$ nor $\sigma(P, x_1)$, we cannot reconstruct $\phi_1$ and $P$ as before. One option is to use the very same coefficient $d_1(\mu)$ to approximate $\phi_1$ and $P$ with

$$\widetilde{\mathcal{J}}_1[\phi_1](\mu) = d_1(\mu)\phi_1(\mu_1) \tag{3.12}$$

and

$$\widetilde{\mathcal{J}}_1[P](\mu) = d_1(\mu)P(\mu_1). \tag{3.13}$$

Then we define

$$J_1[\phi_1, \phi_2, P](\mu) = d_1(\mu) \begin{bmatrix} \phi_1(\mu_1) \\ \phi_2(\mu_1) \\ P(\mu_1) \end{bmatrix} \tag{3.14}$$

as the interpolant of $(\phi_1(\mu), \phi_2(\mu), P(\mu))$.

For subsequent dimensions, we proceed by induction. We assume that, for a given $M > 1$, we have selected $\{\mu_1, \ldots, \mu_M\}$ and we have the set of locations $\{x_1, \ldots, x_M\}$ for the sensors of $\phi_2$. We also assume that the generalized interpolant for $\phi_2$,

$$\mathcal{J}_M[\phi_2](\mu) \coloneqq \sum_{j=1}^{M} d_j(\mu)\phi_2(\mu_j), \tag{3.15}$$

is well defined. The approximation of $(\phi_1(\mu), \phi_2(\mu), P(\mu))$ reads

$$J_M[\phi_1, \phi_2, P](\mu) = \sum_{j=1}^{M} d_j \begin{bmatrix} \phi_1(\mu_j) \\ \phi_2(\mu_j) \\ P(\mu_j) \end{bmatrix}. \tag{3.16}$$

We then define $\mu_{M+1}$ as the parameter which maximizes

$$\max \begin{pmatrix} \max_{\mu\in\mathcal{D}} \frac{\|(\phi_1 - J_M[\phi_1,\phi_2,P]_{\phi_1})(\mu)\|}{\|\phi_1(\mu)\|} \\ \max_{\mu\in\mathcal{D}} \frac{\|(\phi_2 - J_M[\phi_1,\phi_2,P]_{\phi_2})(\mu)\|}{\|\phi_2(\mu)\|} \\ \max_{\mu\in\mathcal{D}} \frac{\|(P - J_M[\phi_1,\phi_2,P]_{P})(\mu)\|}{\|P(\mu)\|} \end{pmatrix}, \tag{3.17}$$

where we use relative errors in order to deal with possible differences in the magnitude orders of $\phi_1$, $\phi_2$ and $P$. Finally, the next sensor location $x_{M+1}$ satisfies

$$|\sigma\left((\phi_2 - \mathcal{J}_M[\phi_2])(\mu_{M+1}), x_{M+1}\right)| = \max_{x\in\mathcal{C}} |\sigma\left((\phi_2 - \mathcal{J}_M[\phi_2])(\mu), x\right)| \tag{3.18}$$

and the inductive step is completed.

Contrary to $\mathcal{J}_n[\phi_2](\mu)$, note that $J_M[\phi_1, \phi_2, P]_{\phi_1}$ and $J_M[\phi_1, \phi_2, P]_P$ are not interpolants of $\phi_1$ and $P$ since they do not satisfy any interpolation condition of the type (2.4). The tilde in the notation of equations (3.12) and (3.13) is there to stress on this fact. However, as we will see in Section 4, the approach yields a good accuracy in the numerical simulations that we have considered. We again emphasize that the same approach was used in [5] in a Stokes problem with a good accuracy in the reconstruction. The reference might be of interest to the community studying thermal-hydraulics in reactor cores.

Before giving some numerical results, a remark on the hypothesis about the bijectivity of the mapping between $\mu \mapsto \phi_2(\mu)$ is in order. Classical results from spectral theory ensure that, for $\mu \in \mathcal{D}$, the mapping $\mu \mapsto (\phi_1, \phi_2)(\mu)$ is one-to-one. However, they do not

ensure bijectivity of the mapping $\mu \mapsto \phi_2(\mu)$. We assume that we are in a parameter regime where this holds because we reconstruct $(\phi_1, \phi_2, P)(\mu)$ from measurements only acquired from thermal flux $\phi_2(\mu)$. If $\mu \mapsto (\phi_1, \phi_2)(\mu)$ is bijective and $\mu \mapsto \phi_2(\mu)$ was not, then we would have existence of $\mu_1 \neq \mu_2$ in $\mathcal{D}$ such that $\phi_2(\mu_1) = \phi_2(\mu_2)$ but $\phi_1(\mu_1) \neq \phi_1(\mu_2)$. This would imply that $\mathcal{J}_M[\phi_2](\mu_1) = \mathcal{J}_M[\phi_2](\mu_2)$ and therefore $J_M[\phi_1, \phi_2, P](\mu_1) = J_M[\phi_1, \phi_2, P](\mu_2)$. As a result, we would have reconstructed $\phi_1(\mu_1)$ and $\phi_1(\mu_2)$ with the same function and the quality of approximation would no longer be ensured.

### *3.3. State-of-the-art on the use of reduced order modelling for nuclear reactor simulations*

We give here a brief state of the art on previous works on nuclear reactor simulations that make use of reduced order modelling techniques. The method which seems to have been more extensively employed is the so called Proper Orthogonal Decomposition (POD [20, 21]). Examples of applications to neutronics are [22] and [23, 24, 25]. In addition to these contributions, one can find in [26] an evaluation of the temperature reactivity feedbacks in a lead-cooled fast reactor with a POD basis.

Less numerous are the contributions using the reduced basis method. The works [27, 28, 29] apply the method to nuclear reactor core spatial kinetics and dynamics. In particular, [30] models the motion of control rods by applying reduced bases to parametrized multi-group neutron diffusion equations both in the time-dependent and stationary formulations. In addition to this, a new numerical algorithm based on reduced basis techniques is proposed in [31] to improve the computational performances for the homogenization of a coupled elliptic-parabolic system describing flows in heterogeneous porous media in nuclear waste storage. As already brought up, our main contribution is to couple the reduced basis techniques with measurement data for monitoring purposes and also for the positionning of sensors in a systematic manner.

## 4. Numerical examples: search for sensor locations for flux and power reconstruction

In Sections 4.1 and 4.2, we reconstruct $\phi_1$, $\phi_2$ and $P$ with the only knowledge of thermal flux measurements. The examples are in one and two dimensions and use the methodology of Section 3.2. For the sensor selection and placement, we consider two cases:

- Case I: the sensors can be placed at any point, in Section 3.2, the partial region $\mathcal{C} = \mathcal{R}$.
- Case II: the admissible sensor locations are restricted to the core $\mathcal{R}_{\text{core}}$, which corresponds to setting $\mathcal{C} = \mathcal{R}_{\text{core}}$ in the algorithm of Section 3.2.

With these two cases, we aim to show how the algorithm can be adapted to explore different restrictions in the positioning of the sensors. In addition to these tests, we present in Section 4.3 a non trivial application to a Pressurized Water Reactor operated by EDF.

*4.1. An example in one dimension*

We consider the classical 1D test case presented in [32, Chapter 4]. The reactor domain is $\mathcal{R} = [0, 30\text{cm}]$. The core and the reflector are $\mathcal{R}_{\text{core}} = [0, 25\,\text{cm}]$ and $\mathcal{R}_{\text{refl}} = [25, 30\,\text{cm}]$ respectively. The parametrized model is the one given in (3.3) with periodic boundary conditions. The discretization with $\mathbb{P}_1$ finite elements uses a mesh of size $h = 0.01\,\text{cm}$. We consider only the value of $D_1|_{\mathcal{R}_{\text{refl}}}$ in the reflector $\mathcal{R}_{\text{refl}}$ as a parameter (so $p = 1$ and $\mu = D_1|_{\mathcal{R}_{\text{refl}}}$). We assume that $D_1|_{\mathcal{R}_{\text{refl}}} \in [0.5, 2.0]$. The rest of the coefficients of the diffusion model (3.1) (including $D_1|_{\mathcal{R}_{\text{core}}}$) are fixed to the values indicated in Table 4.1. In principle, one could also consider these coefficients as parameters but we have decided to focus only on $D_1|_{\mathcal{R}_{\text{refl}}}$ because of its crucial role in the physical state of the core: its variation can be understood as a change in the boundary conditions in $\mathcal{R}_{\text{core}}$ which, up to a certain extent, allows to compensate the bias of the diffusion model with respect to reality.

| | Core | | Reflector | |
|---|---|---|---|---|
| Energy group | 1 | 2 | 1 | 2 |
| $\chi$ | 1.0 | 0.0 | 0.0 | 0.0 |
| $\nu\Sigma_f(\text{cm}^{-1})$ | 0.0085 | 0.1851 | 0.0 | 0.0 |
| $\Sigma_a(\text{cm}^{-1})$ | 0.0121 | 0.121 | 0.0004 | 0.020 |
| $\Sigma_{s,1\to2}(\text{cm}^{-1})$ | 0.0241 | – | 0.0493 | – |
| $D(\text{cm})$ | 1.267 | 0.354 | $\in$ [0.5,2.0] | 0.166 |

Table 4.1: Coefficient values.

In Figure 1 we show some examples of the behavior of $(\phi_1, \phi_2, P)$ for different values of the parameter $D_1|_{\mathcal{R}_{\text{refl}}}$. We confirm visually that $\mu \mapsto \phi_2(\mu)$ is a bijective mapping.

For any $D_1|_{\mathcal{R}_{\text{refl}}} \in [0.5, 2.0]$, we reconstruct $(\phi_1, \phi_2, P)$ as outlined in Section 3.2, that is, we approximate $\phi_2$ with its generalized interpolant $\mathcal{J}_n[\phi_2]$ (see (3.15)) and $\phi_1$ and $P$ with the corresponding components of $J_M[\phi_1, \phi_2, P]$ (see (3.16)). For this, we run the greedy algorithm over a set of 300 snapshots of $(\phi_1, \phi_2, P)$ (solutions of the PDE for a discrete grid $\mathcal{D}^{(\text{training})} \subset \mathcal{D}$ of 300 parameters). We use pointwise evaluations as a model for the sensors. The admissible domain for the search of the interpolating points is either $\mathcal{C} = \mathcal{R}$ (case I) or $\mathcal{C} = \mathcal{R}_{\text{core}}$ (case II).

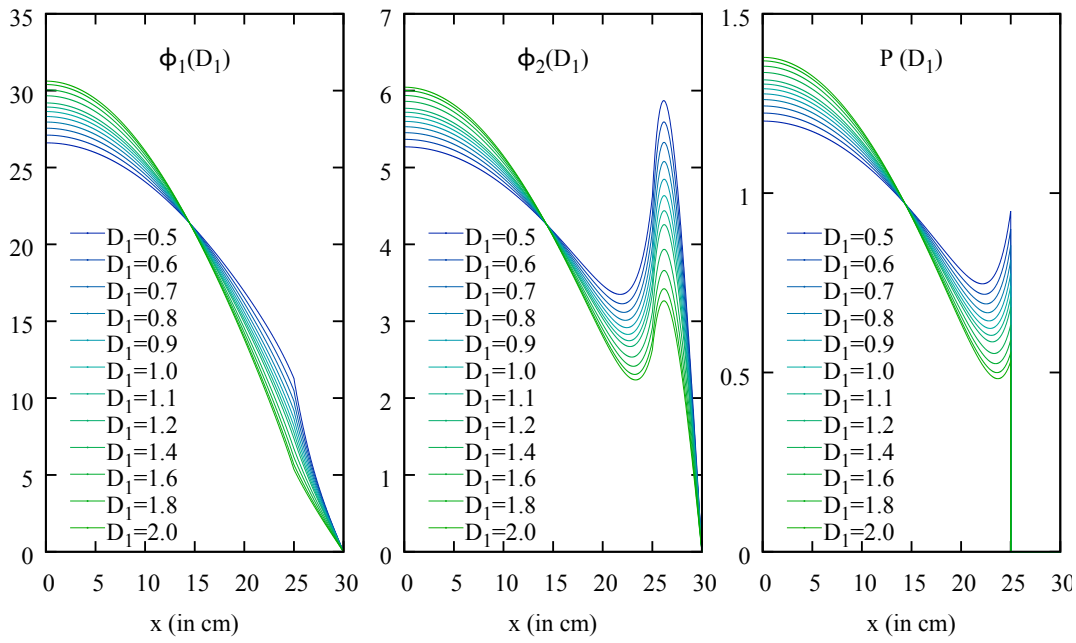


Figure 1: $(\phi_1, \phi_2, P)$ for different values of $D_1|_{\mathcal{R}_{\text{refl}}}$. The values have been normalized to a reference quantity.

Let us now turn to the analysis of the results. We study the performance of the reconstruction strategy by considering first of all the decay of the relative errors

$$\begin{cases} e_n^{(\text{training})}(\phi_1) & := \max_{\mu\in\mathcal{D}^{(\text{training})}} \|\phi_1(\mu) - J_M[\phi_1,\phi_2,P]_{\phi_1}(\mu)\|_{L^2(\mathcal{R})}/\|\phi_1(\mu)\|_{L^2(\mathcal{R})} \\ e_n^{(\text{training})}(\phi_2) & := \max_{\mu\in\mathcal{D}^{(\text{training})}} \|\phi_1(\mu) - J_M[\phi_1,\phi_2,P]_{\phi_2}(\mu)\|_{L^2(\mathcal{R})}/\|\phi_2(\mu)\|_{L^2(\mathcal{R})} \\ e_n^{(\text{training})}(P) & := \max_{\mu\in\mathcal{D}^{(\text{training})}} \|P(\mu) - J_M[\phi_1,\phi_2,P]_{P}(\mu)\|_{L^2(\mathcal{R})}/\|P(\mu)\|_{L^2(\mathcal{R})} \end{cases} \tag{4.1}$$

in the greedy algorithm. In Figures 2a and 2b we plot the decay for case I and II respectively and observe that both yield very similar results. This is possibly due to the simplicity of the example. The decay is compared to an indicator of the optimal performance in $L^2(\mathcal{R})$ which is obtained by a singular value decomposition of the snapshots $\phi_2(\mu),\ \forall\mu\in\mathcal{D}^{(\text{training})}$. We see that $e_n^{(\text{training})}(\phi_2)$ decays at a similar rate as the SVD which suggests that GEIM behaves in a quasi-optimal way (see [10]). We now estimate the accuracy to reconstruct $(\phi_1,\phi_2,P)(D_1|_{\mathcal{R}_{\text{refl}}})$ for parameter values of $D_1|_{\mathcal{R}_{\text{refl}}}\in[0.5,2.0]$ which do not necessary belong to the training set $\mathcal{D}^{(\text{training})}$. For this, we consider a test set of 300 parameters $\mathcal{D}^{(\text{test})}$ different from $\mathcal{D}^{(\text{training})}$ and compute the relative errors

$$\begin{cases} e_n^{(\text{test})}(\phi_1) & := \max_{\mu\in\mathcal{D}^{(\text{test})}} \|\phi_1(\mu) - J_M[\phi_1,\phi_2,P]_{\phi_1}(\mu)\|_{L^2(\mathcal{R})}/\|\phi_1(\mu)\|_{L^2(\mathcal{R})} \\ e_n^{(\text{test})}(\phi_2) & := \max_{\mu\in\mathcal{D}^{(\text{test})}} \|\phi_1(\mu) - J_M[\phi_1,\phi_2,P]_{\phi_2}(\mu)\|_{L^2(\mathcal{R})}/\|\phi_2(\mu)\|_{L^2(\mathcal{R})} \\ e_n^{(\text{test})}(P) & := \max_{\mu\in\mathcal{D}^{(\text{test})}} \|P(\mu) - J_M[\phi_1,\phi_2,P]_{P}(\mu)\|_{L^2(\mathcal{R})}/\|P(\mu)\|_{L^2(\mathcal{R})}. \end{cases} \tag{4.2}$$

Figure 3a shows the decay of these quantities for the first case where $\mathcal{C}=\mathcal{R}$. The behavior is almost identical to the case with $\mathcal{D}^{(\text{training})}$, which suggests that the training set was large

enough for this example (otherwise the decay of the errors on $\mathcal{D}^{(\text{test})}$ might not have followed the same trend). In addition to this, the very fast decay rate of the reconstruction errors for $\phi_1$ and $P$ shows that, in this simple example, it is possible to reconstruct these quantities with measurements of $\phi_2$ only. For certain safety studies, one might be interested in the behavior of the algorithm in $L^\infty(\mathcal{R})$. In this case, very similar results to the $L^2(\mathcal{R})$ norm are observed as Figure 3b shows. Also, the exact same conclusions can be drawn from the results on the second case where $\mathcal{C} = \mathcal{R}_{\text{core}}$ and the plots are not given for the sake of brevity.

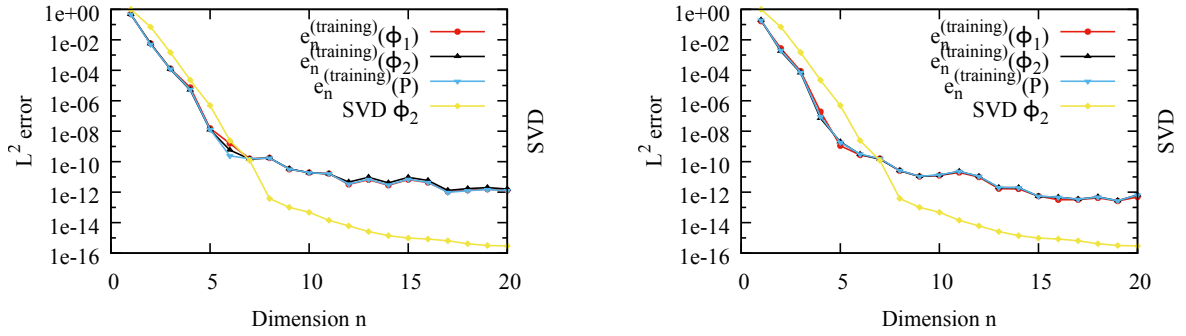


(a) Case I (b) Case II

Figure 2: Relative errors $e_n^{(\text{training})}(\phi_1)$, $e_n^{(\text{training})}(\phi_2)$ and $e_n^{(\text{training})}(P)$ (Cases I and II, $L^2(\mathcal{R})$ norm).

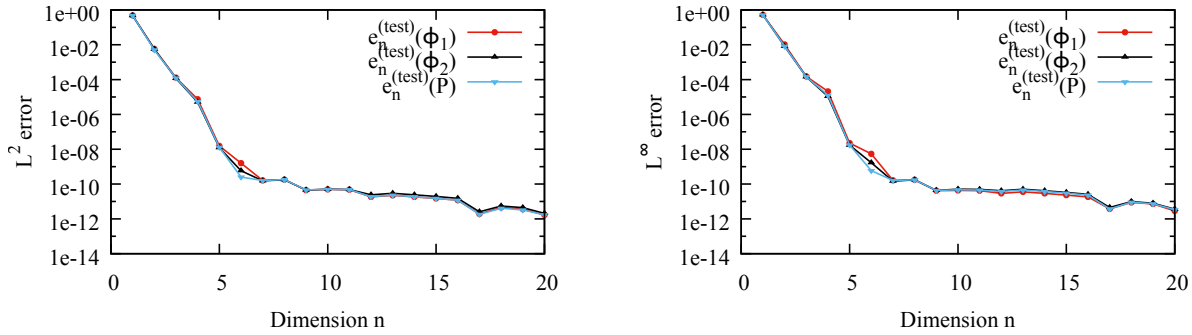


(a) $L^2(\Omega)$ norm (b) $L^\infty(\Omega)$ norm

Figure 3: Reconstruction errors $e_n^{(\text{test})}(\phi_1)$, $e_n^{(\text{test})}(\phi_2)$, $e_n^{(\text{test})}(P)$ (Case I, $L^2(\mathcal{R})$ and $L^\infty(\mathcal{R})$ norms).

As already brought up, the greedy algorithm finds sensor locations that can be used as a systematic tool for sensor placement. The locations selected in this simple test are given in Figures 4a and 4b for both cases I and II. We may note that the first locations (until more or less ten) tend to cluster around the border. This could be seen as an indication that the selection is of good quality.

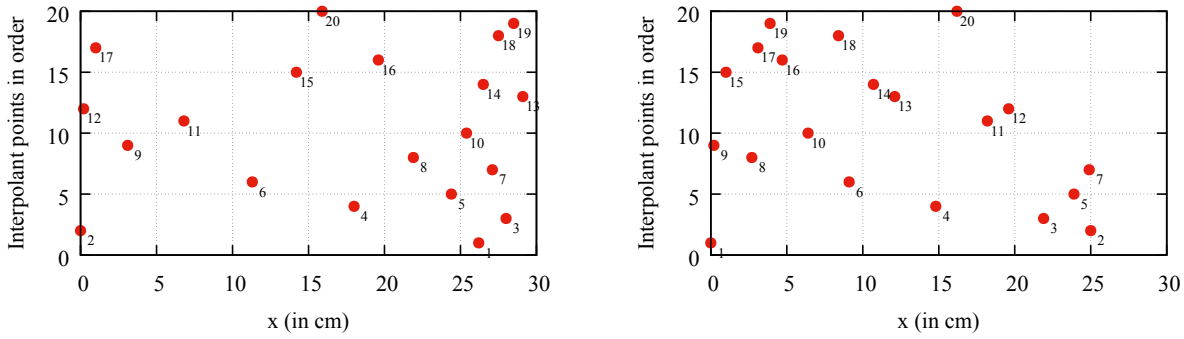


(a) Case I ($\mathcal{C} = \mathcal{R}$) (b) Case II ($\mathcal{C} = \mathcal{R}_{\text{core}}$)

Figure 4: Sensor locations chosen by the greedy algorithm.

*4.2. An example in two dimensions*

We consider the classical 2D IAEA Benchmark Problem (see page 437 of [33] for its official definition and [34, 35] for implementations with different neutronic codes). The reactor geometry is shown in Figure 5. Only one quarter is given because the rest can be inferred by symmetry along the $x$ and $y$ axis.

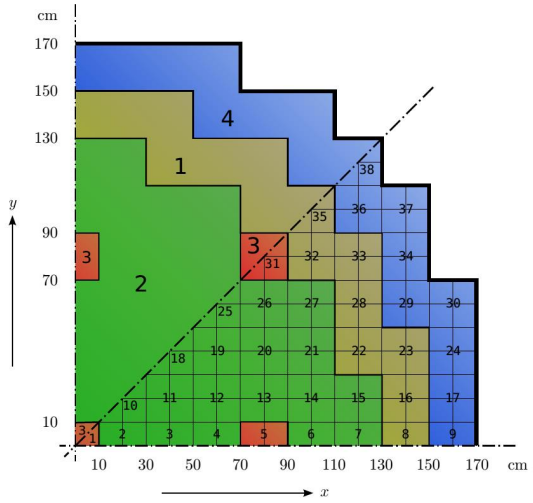


Figure 5: Geometry of 2D IAEA benchmark, upper octant: region assignments, lower octant: fuel assembly identification (from reference [35]).

As in the previous example, the parametrized model is the one given in (3.3). The computational domain $\mathcal{R}$ was not the whole reactor but only the lower octant of Figure 5. Note that four regions are numbered: the first three correspond to the core domain $\mathcal{R}_{\text{core}}$, and the fourth being the reflector domain $\mathcal{R}_{\text{refl}}$. Newmann boundary conditions were enforced in the $x = 0$ and $y = x$ axis and the external border has zero boundary conditions. The discretization with $\mathbb{P}_1$ finite elements uses a mesh of size $h = 1\,\text{cm}$. Like in the previous example, the only parameter is $D_1|_{\mathcal{R}_{\text{refl}}}$ for which we assume that it ranges in $[1.0\,\text{cm}, 3.0\,\text{cm}]$

(the value in the original benchmark being 2.0 cm). The rest of the coefficients of the diffusion model (3.1) (including $D_1|_{\mathcal{R}_{\text{core}}}$) are in accordance with the original benchmark problem. Their values are given in Table 4.2.

| Region | $D_1$ | $D_2$ | $\Sigma_{1\to 2}$ | $\Sigma_{a1}$ | $\Sigma_{a2}$ | $\nu\Sigma_{f2}$ | Material |
|---|---|---|---|---|---|---|---|
| 1 | 1.5 | 0.4 | 0.02 | 0.01 | 0.080 | 0.135 | Fuel 1 |
| 2 | 1.5 | 0.4 | 0.02 | 0.01 | 0.085 | 0.135 | Fuel 2 |
| 3 | 1.5 | 0.4 | 0.02 | 0.01 | 0.130 | 0.135 | Fuel 2 + Rod |
| 4 | [1.0, 3.0] | 0.3 | 0.04 | 0 | 0.010 | 0 | Reflector |

Table 4.2: Parameter values: diffusion coefficients $D_i$ (in cm) and macroscopic cross sections (in $\text{cm}^{-1}$).

Using pointwise evaluations as a model for the sensors and working with a test set of 300 parameters for $\mathcal{D}^{\text{test}}$, we proceed in the same way as in the previous example to obtain convergence errors for $e_n^{(\text{test})}(\phi_1)$, $e_n^{(\text{test})}(\phi_2)$ and $e_n^{(\text{test})}(P)$. They are given in Figures 6 and 7 for both cases I and II and in norms $L^2(\mathcal{R})$ and $L^\infty(\mathcal{R})$. As we can see, the errors decays quickly in all cases, confirming the efficiency of the methodology in this two dimensional case. However, in comparison with the previous 1D example, in order to reach the same reconstruction accuracy the dimension of the reduced space and the number sensors is more or less doubled. The fact that the geometry is more complex and two dimensional is probably the most important factor to explain this observation. We finish this example by giving in Figure 8 the corresponding sensor placement for both cases I and II. We observe that in both cases the locations tend to cluster around the Dirichlet boundary.

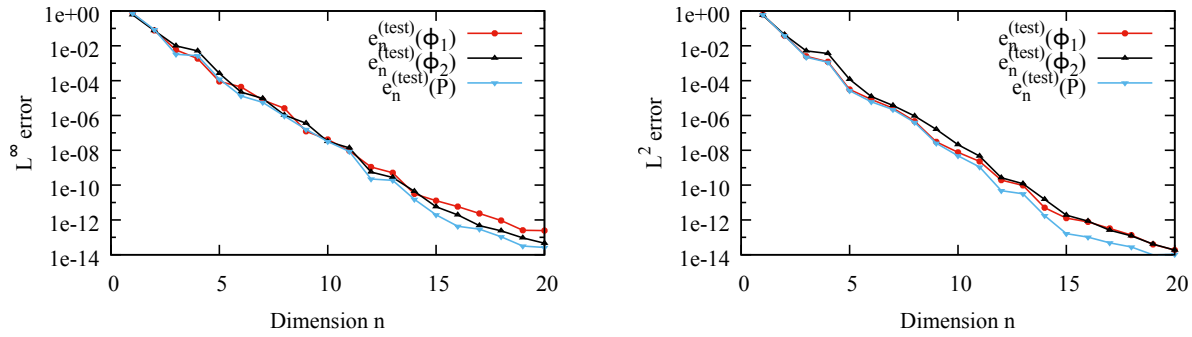


(a) $L^2(\Omega)$ norm (b) $L^\infty(\Omega)$ norm

Figure 6: Case I, error convergence for the reconstruction of $(\phi_1, \phi_2, P)(\mu)$ with $J_M[\phi_1, \phi_2, P](\mu)$ in 2D.

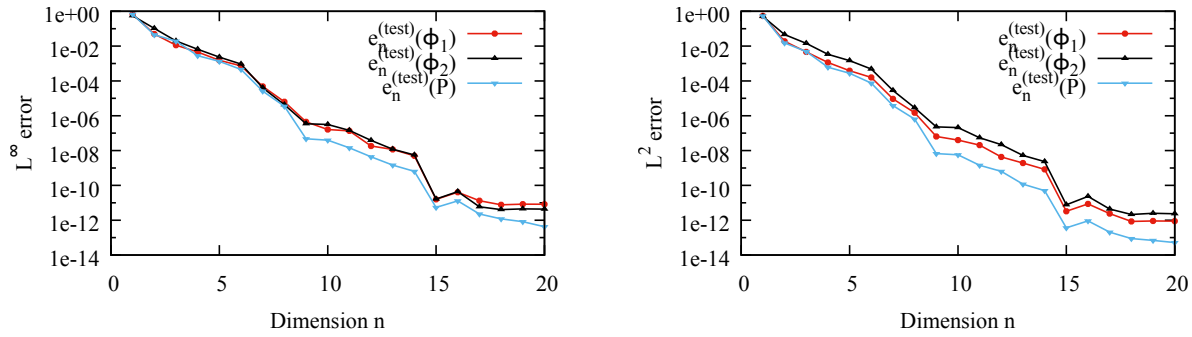


(a) $L^2(\Omega)$ norm (b) $L^\infty(\Omega)$ norm

Figure 7: Case II, error convergence for the reconstruction of $(\phi_1, \phi_2, P)(\mu)$ with $J_M[\phi_1, \phi_2, P](\mu)$ in 2D.

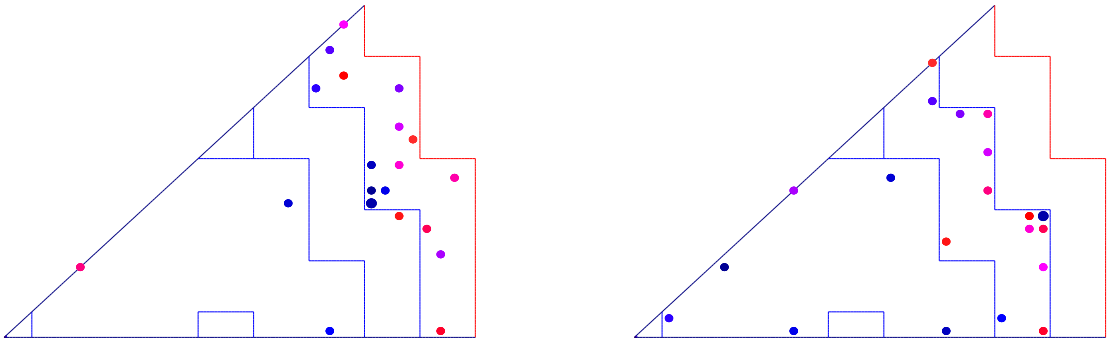

(a) Case I. (b) Case II.

Figure 8: Sensor locations chosen by the greedy algorithm in the 2D example.

### *4.3. Application to a realistic geometry of a PWR operated by EDF*

#### *4.3.1. Problem setting*

We consider a realistic 3D test case involving the core geometry of Pressured Water Reactors of 900, 1300 and 1450 MWe operated by EDF. The geometry for the PWR 900 and 1300 MWe is the one used in reference [36]. For the PWR1450 MWe, we use the one from [37] and an eighth of the core is presented in Figure 9a. Our goal is to find flux sensor locations which are well adapted for the whole life cycle of each reactor. To each time of the life cycle is associated a state of the flux, which is modelled by the solution to problem (3.1) with specific values of the coefficients

$$\mu = \{D_1, D_2, \Sigma_{a,1}, \Sigma_{a,2}, \Sigma_{s,1\to 2}, \nu, \Sigma_{f,1}, \Sigma_{f,2}, \chi_1, \chi_2\}.$$

Here we work with boundary values defined by engineering rules which we do not explain here for the sake of brevity. The entries of $\mu$ vary in space depending on the materials contained in each fuel assembly. Their values also depend on three macroscopic parameters which give the stage of the life cycle:

- $Pw$: the power level of the reactor core. It ranges between 0.3 and 1.
- $Bu$: the average burnup of the fuel in the whole core. It is a measure of how much energy is extracted from the fuel so it is an increasing function in time. It ranges between 0 (for the beginning of the life cycle) and $Bu_{\max}$ (the end of the life cycle) and its exact evolution depends on the operating history of the reactor.
- $D_1|_R$: the diffusion coefficient of the reflector (labelled with an R in Figure 9a). The coefficient follows a classical Lefebvre-Lebigot modelling of the reflector and ranges between 1.0 and 1.6.

Therefore, in this case, $\mu$ depends on the vector of "general" parameters

$$g \coloneqq (Pw, Bu, D_1|_R)$$

that range in

$$\mathcal{G} := [0.3, 1] \times [0, Bu_{max}] \times [1.0, 1.6].$$

So the manifold of solutions is

$$\mathcal{M}_{\phi_1,\phi_2,P} \coloneqq \{(\phi_1, \phi_2, P)(\mu(g)) \ : \ g \in \mathcal{G}\}. \tag{4.3}$$

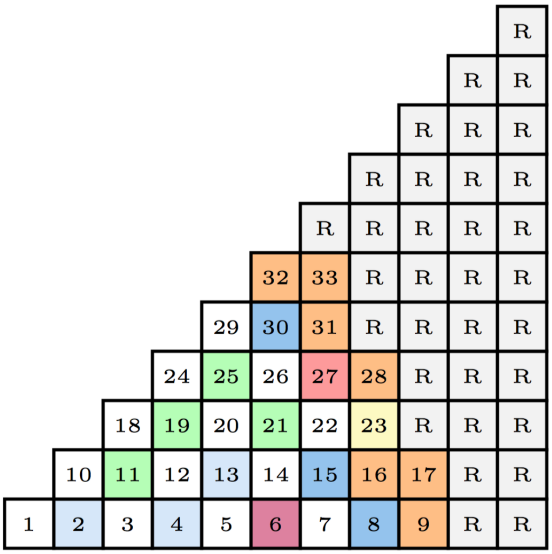


(a) Eighth of core (1-33: fuel assembly; R: reflector).

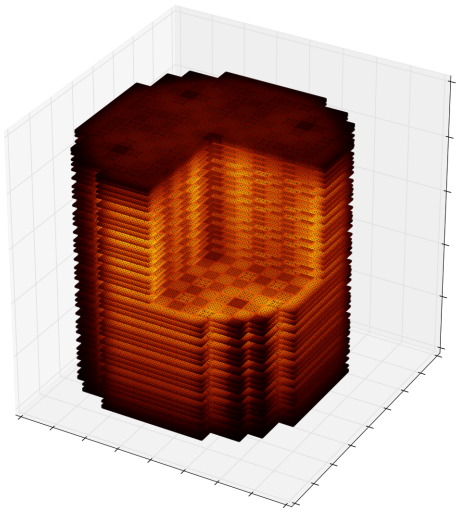

(b) Example of the 3D power distribution over the core from COCAGNE calculation

Figure 9: The fuel assembly loading scheme and an example of 3D power distribution over the core in a realistic 1450 MWe reactor at EDF.

*4.3.2. Selection of assemblies to place the sensors for $\phi_2$*

We have explored two approaches involving GEIM to find sensor locations for $\phi_2$ in each PWR. For technological reasons, their placement is driven by the search of the most convenient assembly to take measurements so the output of our algorithm will be the assemblies where we locate the sensors. Therefore, even if the flux and power are three dimensional, our task can be seen as a 2D sensor placement problem and motivates to explore different strategies which we next explain. In all cases, we have run the greedy algorithms with a training set of 1000 snapshots. They are the solutions associated to a $5 \times 5 \times 40$ uniform grid $\mathcal{G}^{(\text{training})}$ of the parameter set $\mathcal{G}$. Note that we make a finer sampling on $D_1|_R$ because we know that the solutions are more sensitive to this parameter. The snapshots have been generated with COCAGNE [38], an R&D code developped at EDF R&D. We give in Figure 9b an example of the 3D power distribution in the core of the PWR 1450 MWe reactor.

**The 3D2D method:** We run the greedy algorithm of Section 3.2 with:

- the 1000 snapshots in 3D computed with COCAGNE,
- sensors that give local averages of $\phi_2$ over portions of the assemblies that are called *assembly nodes*. Denoting by $A$ the index set of the assemblies and, for each $a \in A$, defining $N(a)$ as the set of assembly nodes in assembly $a$, the measure on an assembly node $n \in N(a)$ is

$$\sigma_n(\phi_2) \coloneqq \frac{\int_{\text{Vol(n)}} \phi_2 \, \mathrm{d}\mathcal{R}}{\text{Vol}(n)}$$

As an example, we give the first 20 locations for the case of the PWR 1450 MWe in Figure 10.

Note that, with this approach, we may select more than one sensor per assembly. As a result, we need to post-process the output of the greedy algorithm in order to decide what are the most suitable assemblies. Our strategy goes as follows. We keep the reduced basis $X_M^2$ computed with the greedy algorithm and compute

$$w_a = \sum_{n \in N(a)} w_n, \quad \forall a \in A,$$

where

$$w_n \coloneqq \max_{g \in \mathcal{G}^{(\text{training})}} |\sigma_n \left(\phi_2(\mu(g)) - \mathcal{J}_M[\phi_2](\mu(g))\right)|.$$

We finally arrange the values $\{w_a\}_{a \in A}$ in decreasing order and choose the assemblies according to this ordering. Figure 11 shows the first 50 assemblies where to place the sensors for the three types of PWR's.

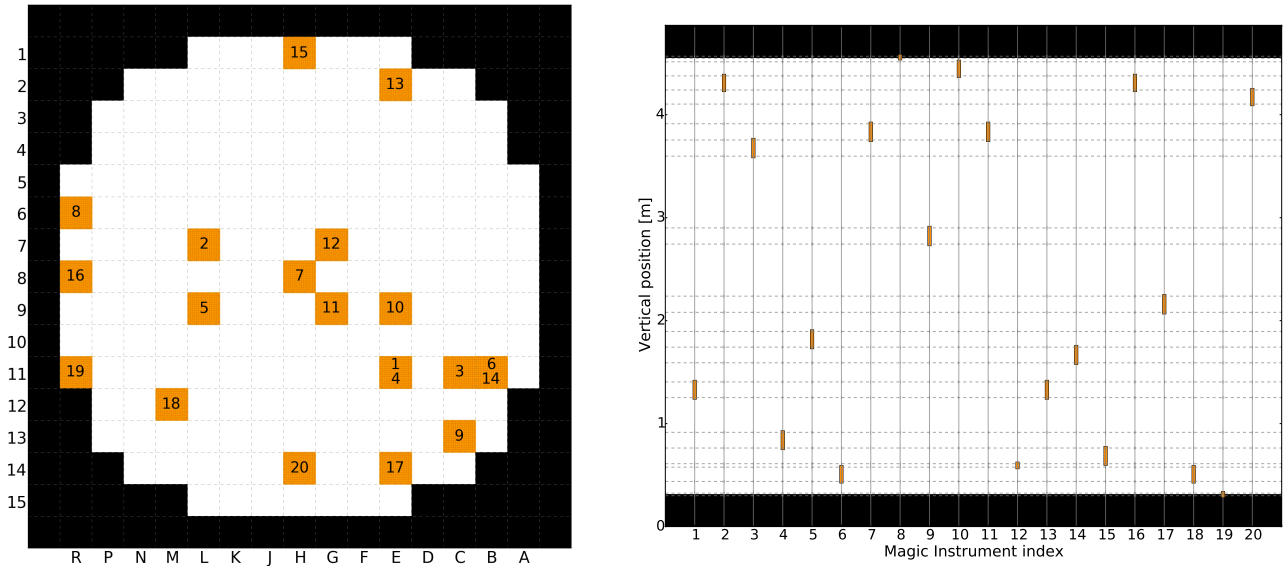


(a) Radial (b) Axial

Figure 10: The first 20 sensors placements, a realistic 1450 MWe reactor.

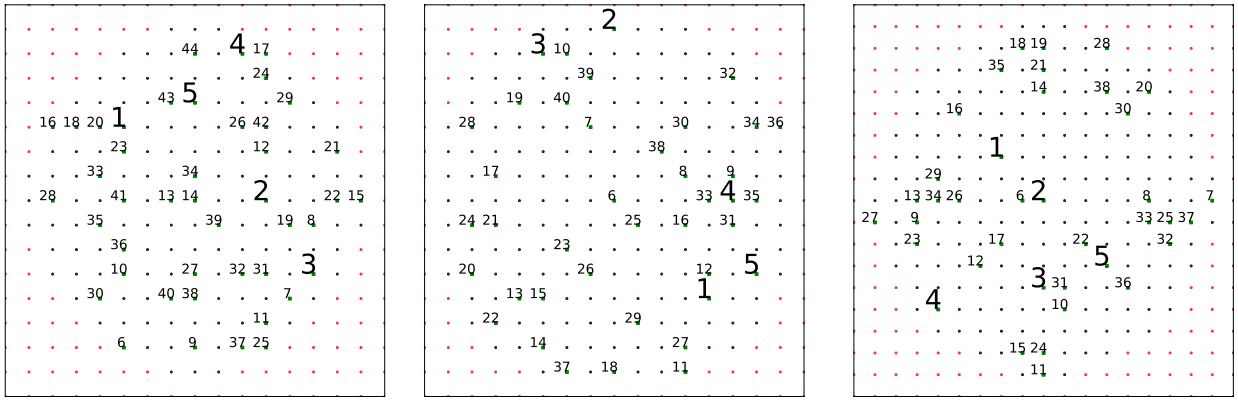

(a) PWR 900 (b) PWR 1300 (c) PWR 1450

Figure 11: 3D2D: The first 50 assemblies to place sensors for PWR 900/1300/1450 MWe reactor cores.

**The 2D2D method:** In this second approach, we integrate the snapshots over the vertical axis and run the greedy algorithm in the resulting 2D fluxes and power distributions. The measurements are averages over the assemblies. This approach gives directly a choice of the assemblies to select without a post-processing phase. Figure 12 shows the first 50 assemblies where to place the sensors for the three types of PWR's.

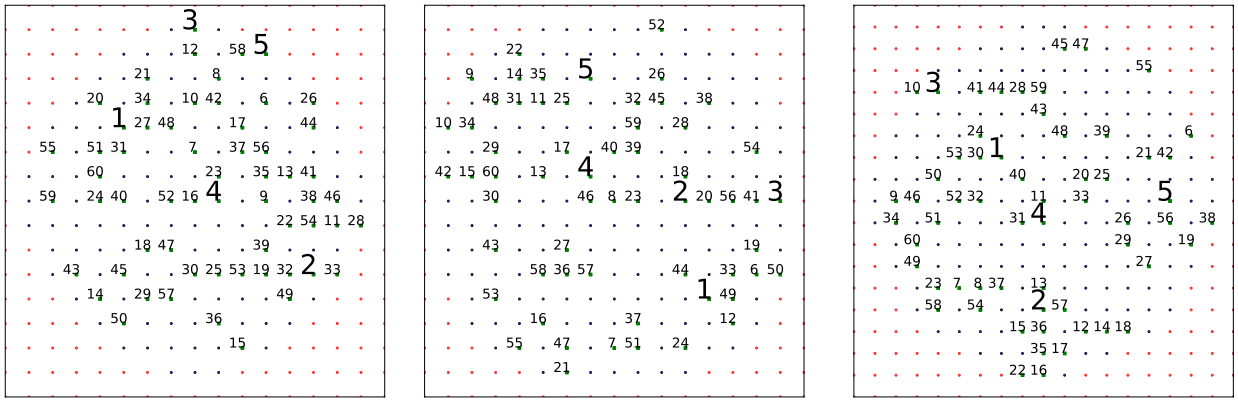

(a) PWR 900 (b) PWR 1300 (c) PWR 1450

Figure 12: 2D2D: The first 50 assemblies to place sensors for PWR 900/1300/1450 MWe reactor cores.

*4.3.3. Analysis of the results*

We first analyze the 3D2D case. From Figure 11, we notice that the mecanisms of sensor placement are pretty similar on the three types of PWR's. Globally speaking, two main areas are instrumented: one at the center of the core and another one at the limit between the core and the reflector. As a result, around the center of the core is a "ring" that is rather free of sensors in the three cases. If we focus on the order in which the first five assemblies are selected, we observe that the first ones are located at the border for the PWR 900 and 1300 MWe and at the center for PWR 1450 MWe.

The selected locations seem physically coherent with the structure of the neutronic flux in the core. The main information to be collected by sensors is the flux level inside the core. To get such information, the best option is to measure close to the center. This gives a good insight of the overall behavior of the core. Then the second global step is to characterize the behavior at the border which informs about the balance effect between the production (at the center) and the leakage (at the border). This explains the placement of the sensors at the border. It can also be linked to the importance, for global neutronic equilibrium in the core, of properly knowing the neutronic behavior at the transition between the reflector and the core. Moreover, these effects are also consistent with the burnup decrease during the whole life cycle of the reactor core, leading to changes in the power distribution and requiring information on each type of neutronic field distribution from the beginning to the end of the cycle. Thus the behavior of the method is in agreement with the neutronic physical expectations.

If we compare globally the sensor placement with the 3D2D and the 2D2D methods, both seem to be rather close. This confirms that working with the axially integrated flux and power is enough to determine the optimal positioning of the instrumental network.

We next study the quality of the reconstruction. From an engineering point of view, the most interesting parameter is the burnup $Bu$ so we focus on its impact in the following. The study is carried out on examples with 5 and 15 instruments. This may seem to be a small number, but if we increase the number of sensors to be similar to real cores, the results

become too close because the amount of information provided is enough. This saturation effect of mandatory information for field reconstruction has already been demonstrated in [39]. Thus, a setup with few sensors is chosen. In order to better evaluate the quality of the optimized sensor locations, we also analyze 100 random instrumental setups. In these random cases, the instrumental setup does not use any knowledge about the interest of each measurement for the overall field quality. This complement is given for all kinds of cores that we are taking into account in this study.

Figure 13 shows the mean reconstruction error over the whole core as a function of the burnup with 5 sensors for the 2D2D and 3D2D methods. The average of the error over the 100 random configurations is also plotted. We notice that the optimized sensor locations based on the greedy algorithm are clearly better than the averaged random ones. Moreover, this effect is the same for all cores. It demonstrates that the greedy algorithm of GEIM is also efficient in practice. We notice that the 3D2D results are a little worse than the 2D2D ones for the three cores. This can be understood in terms of dimension according to the instrumental network. As we look for a 2D network of instrumentation, it seems that the very accurate information we obtain with the 3D case is not fully useful.

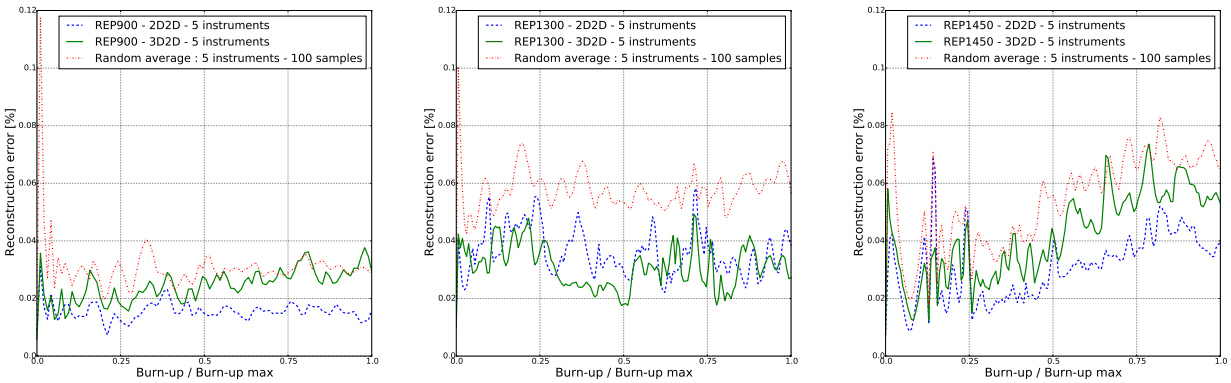


(a) PWR 900 (b) PWR 1300 (c) PWR 1450

Figure 13: Quality of the reconstruction as a function of the burnup for 5 instruments, for PWR 900/1300/1450 MWe reactor cores.

We follow the same lines to analyze the case with 15 sensors. We give results on the field reconstruction in Figure 14. From this figure, we can draw a similar conclusion as with the 5 sensors. The sensor placement proposed with GEIM is better than a random selection. However, when comparing in detail the figures by pairs for the same core type, we notice that the difference between the random placement and the optimal one for 15 instruments is less obvious. Since more information is provided with 15 sensors than with 5, the differences between the random and optimal is less clear. This is even clearer if we compare the 3D2D and 2D2D cases, which are closer with 15 sensors than with only 5. The 2D2D method is still more efficient than the 3D2D method as it fits better with the design of the final instrumental network we aim to build.

Finally, whichever the strategies (3D2D method or 2D2D method) we choose to conden-

sate information into 2D framework, the optimal networks are far better than the averaged random ones. It confirms the efficiency of the method for neutronic instrumental network analysis. Moreover, the 2D2D global method seems to be better suited than the 3D2D one.

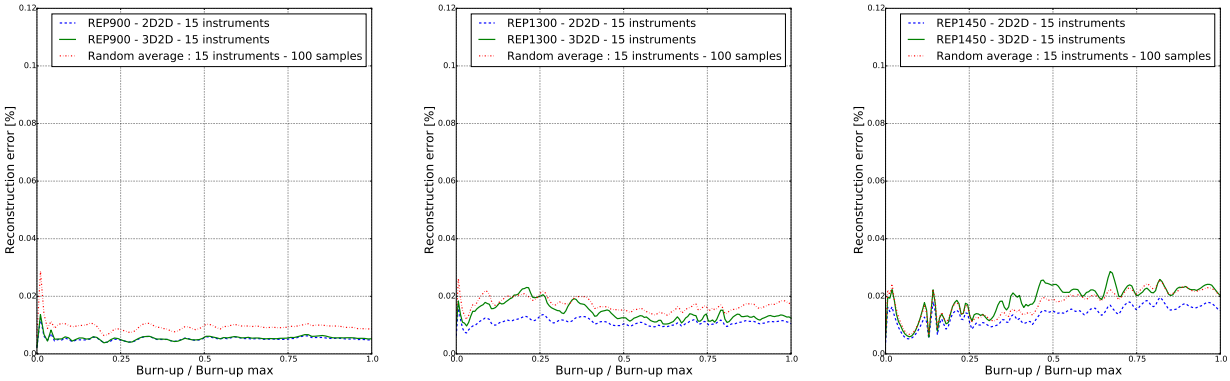


(a) PWR 900 (b) PWR 1300 (c) PWR 1450

Figure 14: Quality of the reconstruction as a function of the burnup for 15 instruments, for PWR 900/1300/1450 MWe reactor cores.

### *4.3.4. Computational cost*

Table 4.3 gives some computational times to illustrate the cost of the greedy algorithm (computed in an offline stage) and the reconstruction with the reduced basis (online stage).

| Items | Off-line | On-line |
|---|---|---|
| A snapshot calculation | 46 | |
| Prepare $\mathcal{M}^{(training)}$, 1000 snapshots | 46110 | |
| Select 50 basis functions and sensors with GEIM greedy algorithm | 20328 | |
| Field reconstruction with 5 basis functions | | 0.05 |
| Field reconstruction with 15 basis functions | | 0.25 |

Table 4.3: Computational cost (in seconds) of GEIM with PWR 1450 MWe reactor core.

## 5. Conclusions and future works

The three examples presented in the paper show how GEIM can be applied to find sensor locations in a reactor core in a systematic way. The example dealing with PWR illustrates the quality of the selection: the locations given by the algorithm yield better reconstruction results than the mean value of a random sampling. This proves that GEIM has the ability to learn the essential mechanisms of the physical system in order to provide good indications on sensor locations. In future works, we will include the deviation of the model with respect to reality by working with PBDW [6]. In this approach, we work with a number of measurements $m \geq n$ and approximate with a least squares projection over the

reduced model $X_n$. The greedy algorithm recently analyzed in [11] could be implemented in order to find optimal locations in this setting.

The current paper works with synthetic measurements and it would be desirable to consider real data but there are still some obstructions to address in the methodology. Current research efforts go into this direction. One of the most important problems to address is that measurements are usually noisy. Some works in this topic whose results could be easily applied to nuclear engineering problems are [40, 41, 42].


[1] J. S. Hesthaven, G. Rozza, and B. Stamm. Certified Reduced Basis Methods for Parametrized Partial Differential Equations. *SpringerBriefs in Mathematics*, 2015.

[2] P. Benner, A. Cohen, M. Ohlberger, and K. Willcox. *Model Reduction and Approximation: Theory and Algorithms*, volume 15. SIAM, 2017.

[3] M. Barrault, Y. Maday, N. C. Nguyen, and A. T. Patera. An empirical interpolation method: application to efficient reduced-basis discretization of partial differential equations. *Comptes Rendus Mathematique*, 339(9):667–672, 2004.

[4] Y. Maday and O. Mula. A Generalized Empirical Interpolation Method: application of reduced basis techniques to data assimilation. In Franco Brezzi, Piero Colli Franzone, Ugo Gianazza, and Gianni Gilardi, editors, *Analysis and Numerics of Partial Differential Equations*, volume 4 of *Springer INdAM Series*, pages 221–235. Springer Milan, 2013.

[5] Y. Maday, O. Mula, A. T. Patera, and M. Yano. The Generalized Empirical Interpolation Method: stability theory on Hilbert spaces with an application to the Stokes equation. *Computer Methods in Applied Mechanics and Engineering*, 287(0):310–334, 2015.

[6] Y. Maday, A. T. Patera, J. D. Penn, and M. Yano. A Parameterized-Background Data-Weak approach to variational data assimilation: formulation, analysis, and application to acoustics. *International Journal for Numerical Methods in Engineering*, 102(5):933–965, 2015.

[7] B. Peherstorfer and K. Willcox. Dynamic data-driven reduced-order models. *Computer Methods in Applied Mechanics and Engineering*, 291:21–41, 2015.

[8] P. Binev, A. Cohen, W. Dahmen, R. DeVore, G. Petrova, and P. Wojtaszczyk. Data assimilation in reduced modeling. *SIAM/ASA Journal on Uncertainty Quantification*, 5(1):1–29, 2017.

[9] R. DeVore, G. Petrova, and P. Wojtaszczyk. Data assimilation in Banach spaces. *arXiv preprint arXiv:1602.06342*, 2016.

[10] Y. Maday, O. Mula, and G. Turinici. Convergence analysis of the Generalized Empirical Interpolation Method. *SIAM Journal on Numerical Analysis*, 54(3):1713–1731, 2016.

[11] P. Binev, A. Cohen, O. Mula, and J. Nichols. Greedy algorithms for optimal measurements selection in state estimation using reduced models. preprint, November 2017.

[12] H. Gong, J.-P. Argaud, B. Bouriquet, and Y. Maday. The Empirical Interpolation Method applied to the neutron diffusion equations with parameter dependence. In *Proceedings of PHYSOR*, 2016.

[13] A. Kolmogoroff. Über die beste Annäherung von Funktionen einer gegebenen Funktionenklasse. *Annals of Mathematics*, 37:107–110, 1936.

[14] Y. Maday, A. T. Patera, and G. Turinici. A priori convergence theory for reduced-basis approximations of single-parameter elliptic partial differential equations. *Journal of Scientific Computing*, 17(1-4):437–446, 2002.

[15] A. Cohen and R. DeVore. Kolmogorov widths under holomorphic mappings. *IMA Journal of Numerical Analysis*, 36(1):1–12, 2015.

[16] A. Cohen and R. DeVore. Approximation of high-dimensional parametric PDEs. *Acta Numerica*, 24:1–159, 2015.

[17] Y. Maday and B. Stamm. Locally adaptive greedy approximations for anisotropic parameter reduced basis spaces. *SIAM Journal on Scientific Computing*, 35(6):A2417–A2441, 2013.

[18] A. Hebert. *Applied Reactor Physics*. Presses inter Polytechnique, 2009.

[19] R. Dautray and J.-L. Lions. *Mathematical Analysis and Numerical Methods for Science and Technology: Volume 6 Evolution Problems II*. Springer Science & Business Media, 2012.

[20] K. Pearson. On Lines and Planes of Closest Fit to Systems of Points in Space. *Philosophical Magazine*, 2:559–572, 1901.

[21] A. Quarteroni, G. Rozza, and A. Manzoni. Certified reduced basis approximation for parametrized partial differential equations and applications. *Journal of Mathematics in Industry*, 1(1):1–49, 2011.

[22] F. Wols, D. Lathouwers, and W. Uyttenhove. Transient analyses of accelerator driven systems using modal expansion techniques. Master's thesis, Delft University of Technology, 2010.

[23] A. G. Buchan, C. C. Pain, F. Fang, and I. M. Navon. A POD reduced-order model for eigenvalue problems with application to reactor physics. *International Journal for Numerical Methods in Engineering*, 95(12):1011–1032, 2013.

[24] A. G. Buchan, A. A. Calloo, M. G Goffin, S. Dargaville, F. Fang, C. Pain, and I. M. Navon. A POD reduced order model for resolving angular direction in neutron/photon transport problems. *Journal of Computational Physics*, 296:138–157, 2015.

[25] C. E. Heaney, A. G. Buchan, C. C. Pain, and S. Jewer. A reduced order model for criticality problems in reactor physics varying control rod settings. In *Proceedings of the 24th UK Conference of the Association for Computational Mechanics in Engineering, Cardiff University, Cardiff*, 2016.

[26] S. Lorenzi, A. Cammi, and L. Luzzi. Spatial neutronics modelling to evaluate the temperature reactivity feedbacks in a lead-cooled fast reactor. *Proceedings of ICAPP 2015, Nice, France, May 03-06*, 2015.

[27] A. Sartori, D. Baroli, A. Cammi, D. Chiesa, L. Luzzi, R. Ponciroli, E. Previtali, M. E. Ricotti, G. Rozza, and M. Sisti. Comparison of a Modal Method and a Proper Orthogonal Decomposition approach for multi-group time-dependent reactor spatial kinetics. *Annals of Nuclear Energy*, 71:217–229, 2014.

[28] A. Sartori. *Reduced order methods: applications to nuclear reactor core spatial dynamics*. PhD thesis, Italy, 2015.

[29] A. Sartori, A. Cammi, L. Luzzi, M. E. Ricotti, G. Rozza, et al. Reduced Order Methods: Applications to Nuclear Reactor Core Spatial Dynamics. In *ICAPP 2015*, pages 3318–3327. Omnipress, 2015.

[30] A. Cammi, L. Luzzi, and G. Rozza. A Reduced Basis Approach for Modeling the Movement of Nuclear Reactor Control Rods. *Journal of Nuclear Engineering and Radiation Science APRIL*, 2:021019–1, 2016.

[31] A. Gloria, T. Goudon, and S. Krell. Numerical homogenization of a nonlinearly coupled elliptic–parabolic system, reduced basis method, and application to nuclear waste storage. *Mathematical models and methods in applied sciences*, 23(13):2523–2560, 2013.

[32] W. M. Stacey. *Nuclear Reactor Physics*. John Wiley & Sons, 2001.

[33] Benchmark Problem Book. ANL-7416, Suppl.2. Argonne National Laboratory, 1977.

[34] PARCS. IAEA 3D PWR problem. `https://engineering.purdue.edu/PARCS/Code/TestSuite/CalculationMode/StandAloneMode/Eigenvalue/IAEA3DPWR`.

[35] G. Theler, F.J. Bonetto, and A. Clausse. Solution of the 2D IAEA PWR Benchmark with the neutronic code Milonga. *Actas de la Reunión Anual de la Asociación Argentina de Tecnología Nuclear, XXXVIII*, 2011.

[36] B. Bouriquet, J.-P. Argaud, P. Erhard, and A. Ponçot. Nuclear core activity reconstruction using heterogeneous instruments with data assimilation. *EPJ Nuclear Sciences & Technologies*, 1:18, 2015.

[37] T. Clerc, A. Hébert, H. Leroyer, J.-P. Argaud, and A. Bouriquet, B.and Ponçot. An advanced computational scheme for the optimization of 2D radial reflector calculations in pressurized water reactors. *Nuclear Engineering and Design*, 273:560–575, 2014.

[38] A. Calloo, D. Couyras, F. Fécotte, and M. Guillo. Cocagne: EDF new neutronic core code for ANDROMEDE calculation chain. In *Proceedings of International Conference on Mathematics & Computational Methods Applied to Nuclear Science & Engineering (M&C), Jeju, Korea*, 2017.

[39] B. Bouriquet, J.-P. Argaud, P. Erhard, S. Massart, A. Ponçot, S. Ricci, and O. Thual. Robustness of nuclear core activity reconstruction by data assimilation. *Journal of Power and Energy Systems*, 6(2):289–301, 2012.

[40] Y. Maday, A. T. Patera, J. D. Penn, and M. Yano. PBDW State Estimation: Noisy Observations; Configuration-Adaptive Background Spaces, Physical Interpretations. *ESAIM: Proceedings and Surveys*, 50:144–168, 2015.

[41] J.-P. Argaud, B. Bouriquet, H. Gong, Y. Maday, and O. Mula. Stabilization of (G)EIM in Presence of Measurement Noise: Application to Nuclear Reactor Physics. In Marco L. Bittencourt, Ney A. Dumont, and Jan S. Hesthaven, editors, *Spectral and High Order Methods for Partial Differential Equations ICOSAHOM 2016: Selected Papers from the ICOSAHOM conference, June 27-July 1, 2016, Rio de Janeiro, Brazil*, pages 133–145. Springer International Publishing, 2017.

[42] T. Taddei. An adaptive parametrized-background data-weak approach to variational data assimilation. *ESAIM: Mathematical Modelling and Numerical Analysis*, 51(5):1827–1858, 2017.